M. Greiner
ASME Mem.
Professor of Mechanical Engineering,
University of Nevada,
Reno, NV 89557
e-mail: greiner@unr.edu

P. F. Fischer
Mathematics and Computer Science Division,
Argonne National Laboratory,
Argonne, IL 60439
e-mail: fischer@mcs.anl.gov

H. M. Tufo
Department of Computer Science,
University of Chicago,
Chicago, IL 60637
e-mail: hmt@cs.uchicago.edu

Two-Dimensional Simulations of Enhanced Heat Transfer in an Intermittently Grooved Channel

Two-dimensional Navier-Stokes simulations of heat and momentum transport in an intermittently grooved passage are performed using the spectral element technique for the Reynolds number range 600≤Re≤1800. The computational domain has seven contiguous transverse grooves cut symmetrically into opposite walls, followed by a flat section with the same length. Periodic inflow/outflow boundary conditions are employed. The development and decay of unsteady flow is observed in the grooved and flat sections, respectively. The axial variation of the unsteady component of velocity is compared to the local heat transfer, shear stress and pressure gradient. The results suggest that intermittently grooved passages may offer even higher heat transfer for a given pumping power than the levels observed in fully grooved passages. [DOI: 10.1115/1.1459730]

Keywords: Channel Flow, Computational, Enhancement, Forced Convection, Instability

Introduction

Engineering devices frequently employ enhanced heat transfer surfaces [1]. Fins are typically used to extend surface areas while offset strips are commonly used to promote thin boundary layers. In recent years, a number of configurations that increase fluid mixing by triggering flow instabilities have been considered. Transversely grooved channel [2–5] passages with eddy promoters [6,7] and communicating channels [8] all contain fairly large features whose sizes are roughly half the channel wall to wall spacing. These structures are designed to excite normally damped Tollmien-Schlichting waves at moderately low Reynolds numbers.

The current authors have presented a series of articles on heat transfer augmentation in rectangular cross section passages with contiguous grooves cut into the walls. Experimental flow visualizations in a long grooved channel downstream of a laminar flat passage show that two-dimensional waves appear after an initial quiescent development length [9]. Unsteadiness is first observed thirty-five hydraulic diameters downstream of the first groove at a Reynolds number of Re=350. As the Reynolds number is increased, the onset moves upstream and the flow behavior at a given location becomes increasingly three-dimensional. Experimental and numerical results in a passage with eddy promoters indicate that the instability that leads to unsteady flow is convective rather than absolute in nature [10]. Measurements using air show that fully developed heat transfer is enhanced relative to laminar flat channel flow by as much as a factor of 4.6 at equal Reynolds numbers and by a factor of 3.5 at equal pumping powers [11,12].

Numerical simulations of fully developed convection in transversely grooved passages were performed using the spectral element technique for Re≤2000 [13,14]. Those simulations employed three-dimensional computational domains that represented one periodicity cell of the contiguously grooved passage. The pressure gradient and heat transfer results were within 20 percent of the measured values. At Re=1000 *two*-dimensional simulations gave Nusselt number values that were 20 percent below *three*-dimensional results while friction factors were smaller by a factor of two. This suggests that three-dimensionality strongly affects the transport characteristics of these flows, especially drag.

Experimental measurements in a flat passage downstream of a grooved channel were performed for Reynolds number range 1500≤Re≤5000 [15,16]. These measurements show that the heat transfer coefficient remained high for a substantial distance in the flat region. The pressure gradient dropped down to the flat passage value much more rapidly, especially for Re>2500. As a result, the heat transfer for a given pumping power was even greater in the first five hydraulic diameters of the decay region than in the grooved passage itself.

Three-dimensional Navier-Stokes simulations in a flat passage downstream of a *fully developed* grooved channel were performed for 405≤Re≤764 [17]. The grooved channel had transverse grooves cut symmetrically into both walls. Two different computational sub-domains were employed. The first represented one periodicity cell of a continuously grooved passage. It had periodic inflow/outflow boundary conditions in order to simulate fully developed flow. The second sub-domain consisted of a single groove cell coupled to a flat passage at the downstream end. The inflow conditions to the grooved/flat sub-domain were taken from the outflow of the fully developed domain. Unsteady flow from the grooved region persisted several groove-lengths into the flat passage. This unsteadiness increased both local heat transfer and pressure gradient relative to steady flat passage flow. Moreover, the heat transfer for a given pumping power in the first three groove-lengths of the flat passage was even greater than the high levels observed in a fully developed grooved passage. However, the numerical Nusselt number decayed more rapidly in the flat passage than was expected from measurements.

The favorable heat transfer versus pumping power performance of flat passages downstream from grooved channels suggests that intermittently grooved passages, in which flat regions separate grooved sections, may have significant advantages in engineering heat transfer devices. However, the development of unsteady flow in grooved regions as well as the decay of unsteady flow exiting from a short grooved section must be investigated before the design of intermittently grooved passages can be optimized.

The current work is a two-dimensional numerical investigation of heat transfer in an intermittently grooved passage for the Reynolds number range 600≤Re≤1800. The grooved portions of this passage have seven right-triangular slots cut symmetrically into opposite walls. The flat portion is also seven groove-lengths long

Contributed by the Heat Transfer Division for publication in the JOURNAL OF HEAT TRANSFER. Manuscript received by the Heat Transfer Division February 6, 2001; revision received October 17, 2001. Associate Editor: M. Faghri.

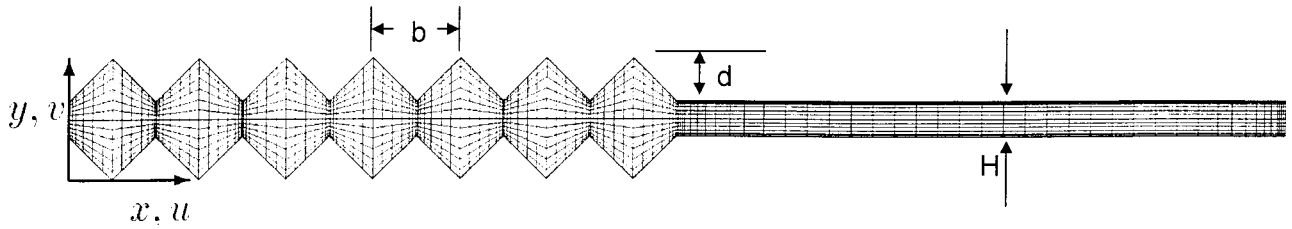

Fig. 1 Computational domain and spectral element mesh

and its wall to wall spacing is the same as the minimum spacing in the grooved section. The study of an intermittently grooved passage requires a very long computational domain. As pointed out earlier, three-dimensional simulations predict the pressure gradient in fully developed grooved passages much more accurately than two-dimensional calculations [13,14]. However, the resources to perform three-dimensional simulations in this large domain are not available at the current time. The current two-dimensional simulations afford an opportunity to learn more about this flow and provide guidance to future three-dimensional calculations.

Numerical Method

Computational Domain. Figure 1 shows the two-dimensional spectral element mesh employed in this work. The upper and lower boundaries are solid walls, and the flow is from left to right. The domain consists of seven grooves, each of length $b=0.024$ m and depth $d=0.012$ m, followed by a flat section of length $7b$. The total domain length is $L_d=14b$ and the minimum passage wall to wall spacing is $H=0.01$ m. The groove length, b, was chosen to be compatible with the wavelength of the most slowly decaying Tollmien-Schlichting waves of the outer channel flow [2]. Moreover, the groove and passage wall to wall dimensions are the same as the geometries studied in our earlier work on decaying unsteadiness downstream of a grooved passage [12,16,17]. However, the current domain uses periodic inlet/outlet boundary conditions and thus models fully developed flow in an *array* of alternating grooved and flat channels.

In the spectral element method [18,19] the velocity, data and geometry are expressed as tensor-product polynomials of degree N in each of K quadrilateral spectral elements, corresponding to a total grid point count of roughly KN^2. Numerical convergence is achieved by increasing the spectral order N. The present calculations were carried out at a base resolution of $K=1960$, $N=7$ (Fig. 1 shows the K spectral elements but not the KN^2 grid points). Resolution tests were performed for $\mathrm{Re}=1200$ and $\mathrm{Re}=1800$ at $N=8$ and $N=9$, respectively. The present simulations use consistent approximation spaces for velocity and pressure, with pressure represented as polynomials of degree $N-2$ [19,20]. The momentum equations are advanced by first computing the convection term, followed by a linear Stokes solve for the viscous and pressure terms. The decoupling allows for convective Courant numbers greater than unity while maintaining second-order accuracy in time. Full details of the method can be found in [20].

The Periodic Domain. The flow is driven from left to right in the periodic domain by applying a uniform body force. The level of forcing is adjusted at each time step to ensure that the mass flow rate through the domain is invariant with time. The approach is outlined in Ghaddar et al. [21] and Fischer and Patera [22]. It exploits the linearity of the implicit Stokes problem. One first computes, in a preprocessing step, velocity and pressure fields for the Stokes problem that result from application of unit forcing, corresponding to a mean pressure gradient, in the absence of nonlinear terms. Then, at each time step, the implicit Stokes problem is solved with the nonlinear terms treated explicitly, in the absence of any mean pressure gradient. To this second solution, we add a multiple of the first that yields the desired flow rate. The multiplier corresponds to the mean pressure gradient.

The thermal problem for the periodic domain requires careful treatment. If one simply specifies zero-temperature conditions on the walls then the solution eventually decays to zero. To produce the desired spatially fully-developed state requires that the temperature profiles at the inlet and outlet be self-similar, that is,

$$T(x=L_d,y,t)=C\,T(x=0,y,t), \tag{1}$$

with $T\geqslant 0$ and $C<1$. The solution technique for computing the fully developed temperature field for constant temperature boundary conditions follows the analysis of Patankar et al. [23]. The energy equation (neglecting viscous dissipation) and associated initial and boundary conditions are

$$\frac{\partial T}{\partial t}+\vec{U}\cdot\nabla T=\alpha\cdot\nabla^2 T \tag{2a}$$

$$T(x,y,t=0)=T_{\mathrm{init}}(x,y) \tag{2b}$$

$$T(x,y,t)=0 \ \text{ on the walls} \tag{2c}$$

$$T(x=L_d,y,t)=e^{-cL_d}T(x=0,y,t) \tag{2d}$$

where $\vec{U}=(u,v)$ is the convecting velocity field determined by the hydrodynamic part of the computation. Equation $(2d)$ corresponds to the fully developed condition where the temperature profile is self-similar in each successive domain in the periodic sequence, that is $T(x+L_d,y,t)=e^{-cL_d}T(x,y,t)$ for all (x,y,t), where $e^{-cL_d}=C$. The constant c is unknown and is a parameter to be determined as part of the computation. The fact that each domain independently satisfies the homogeneous set in Eq. (2) and that we are considering fully developed solutions that are independent of T_{init} implies that the solution to Eq. (2) for each domain would yield the same value of c. Hence, c cannot be a function of x. Moreover, an energy balance on the computational domain shows that c is proportional to the log-mean Stanton number. Since the Stanton number is constant c is not function of time even when the flow is itself unsteady.

Any function satisfying the above self-similar condition has the unique decomposition $T(x,y,t)=e^{-cx}\theta(x,y,t)$, where $\theta(x+L_d,y,t)=\theta(x,y,t)$ is a periodic function. Thus, the computation of T is reduced to the computation of the periodic function θ, and the constant c. Substituting this decomposition into Eq. (2) yields:

$$\frac{\partial\theta}{\partial t}+\vec{U}\cdot\nabla\theta-\alpha\cdot\nabla^2\theta=(\alpha\cdot c^2+uc)\theta-2\alpha\cdot c\frac{\partial\theta}{\partial x} \tag{3a}$$

$$\theta(x,y,t=0)=\theta_{\mathrm{init}}(x,y) \tag{3b}$$

$$\theta(x,y,t)=0 \ \text{ on the walls} \tag{3c}$$

$$\theta(x=L_d,y,t)=\theta(x=0,y,t) \tag{3d}$$

Since the fully developed solution is independent of the initial condition we may arbitrarily assign θ_{init}, which is typically set to unity when starting from rest, or to a prior converged result when

PROOF COPY 007203JHR

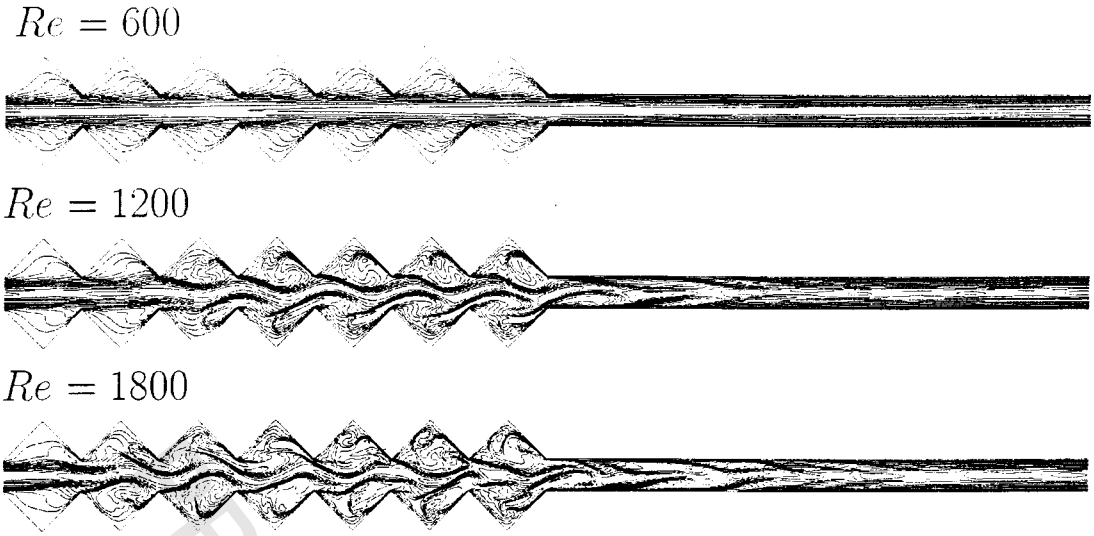

Fig. 2 Snapshot contour plots of periodic temperature θ at Re=600, 1200 and 1800

starting from an existing flow-field. Equation (3*a*) is solved using a semi-implicit time-stepping procedure similar to that of our Navier-Stokes solver. The diffusive terms are treated implicitly while the convective terms are treated explicitly. In addition, all terms on the right of Eq. (3*a*) are treated explicitly using the latest available value for c.

In the steady state case ($\partial/\partial t=0$), Eq. (3) constitutes an eigenproblem for the eigenpair (c,θ). The constant c corresponds to the decay rate of the mean temperature in the x-direction. As such, a larger value of c implies more rapid decay and more effective heat transfer (larger Stanton number). In the convection-dominated limit where the Peclet number $U_m D_h/\alpha$ is large, Eq. (3*a*) becomes a linear eigenvalue problem. In this case, standard iterative methods for computing the lowest value of c (corresponding to the most slowly decaying mode in x) can be used even when the nonlinear (c^2) term in Eq. (3*a*) is not identically zero. We find that this method accurately computes the decay rate and Nusselt numbers for steady flows in square and round ducts [24].

For steady-periodic flows with period τ, the temperature is periodic in time, implying $T(x,y,t+\tau)=T(x,y,t)$. Since c is independent of time, this implies that $\theta(x,y,t+\tau)=\theta(x,y,t)$. If the value of c is not chosen correctly, this condition will not be satisfied. Unfortunately, τ is not known a priori but is a result of the hydrodynamic part of the calculation. A robust approach to computing c is obtained by multiplying Eq. (3*a*) by θ, integrating over the domain Ω, and simplifying to yield:

$$\frac{1}{2}\frac{d}{dt}\int_\Omega \theta^2 dV=\int_\Omega [(\alpha c^2+uc)\theta^2-\alpha\nabla\theta\cdot\nabla\theta]dV \qquad (4)$$

While we do not expect the time derivative of the average temperature (represented by the left-hand side of Eq. (4)) to be identically zero, it will in general be less than the time derivative of θ at any one point in the domain. Moreover, if we integrate the right-hand side of Eq. (4) from time t to $t+\tau$, the resultant quantity must be zero due to the temporal periodicity.

This suggests a two-tier strategy for computing c in the unsteady case. Initially, we determine c such that the right hand side of Eq. (4) is identically zero at each time step. This permits a relatively coarse but quick determination of c and θ. Once τ is well established, we use this value of c to advance θ for one or more periods, and monitor the decay or growth of $\int\theta^2\,dV$. At the end of each trial period, we adjust c until convergence is attained. Typical values of cL_d over the range of Re considered are 0.55 to 1.0, corresponding to 55 percent to 63 percent drops in mean temperature over the domain length.

The simulations at Re=600 were initialized using $u=0$ and $\theta=1$. Subsequent cases were initialized from converged results at lower Reynolds numbers. Because of the extreme length of the domain (14*b*, versus *b* for our earlier computations [13,14]), very long time integrations were required to reach a quasi-steady-periodic state at the higher Reynolds numbers. For example, the Re=1800 case was initiated from the Re=1200 final solution and run for a physical time of 2.9 sec (corresponding to 9.6 convective passages through the domain based on mean flow-rate and domain length) before ''steady state'' statistics were calculated. The statistics were calculated based on a simulation with spectral order $N=9$ and a time step of 0.000016 sec (corresponding to a convective Courant number of 3.0). Solution files were extracted every 100 time steps, and a total of 580 such files were used to compute the time-averaged and rms data. This sampling rate corresponds to roughly 50 samples per oscillation in the solution signal.

Adequacy of the spatial resolution was determined by comparing the results for the most difficult case (Re = 1800) computed using polynomial order $N=7$ with those obtained using $N=9$. Figures 4 and 5 show the axial variations of the fluctuating velocity and the bulk Nusselt number. The results for $N=7$ and 9 are virtually indistinguishable. The maximum difference in the fluctuating velocity is less than 4 percent of the average value. The Nusselt number is based on the *derivative* of temperature. The maximum difference is always less than 3 percent, except at the singular points located at the groove peaks. Given the unsteady nature of these flows, this close agreement indicates both adequate spatial resolution and sufficiently long time integration to obtain meaningful statistics.

The simulations were performed on 8, 16, and 32 processors of a 96 processor SGI Origin2000. Each processor is a MIPS R10000 running at 250 MHz and shares 24 GB of memory. The Re=1800, $N=9$ computation required 2.5 CPU sec/step on 32 nodes.

Results

Figure 2 shows three contour plots of the dimensionless periodic temperature θ. These plots are typical snapshots at Reynolds numbers Re=600, 1200, and 1800. In this work the Reynolds number is Re=$U_m D_H/\nu$. The average velocity through the mini-

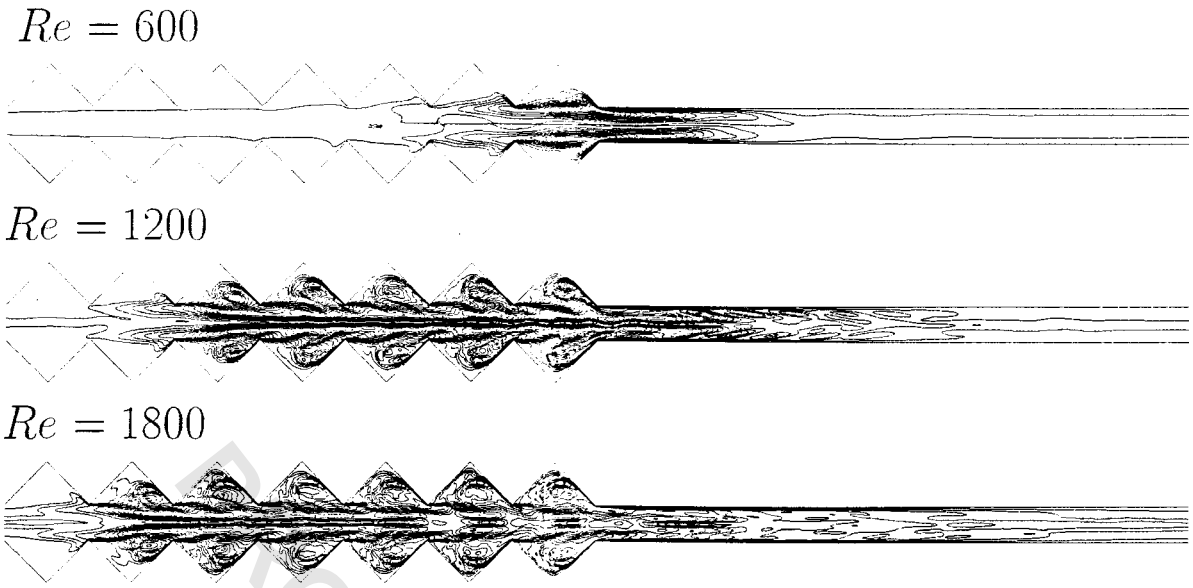

Fig. 3 Contour plots of the root-mean-squared component of periodic temperature θ_{rms} at Re=600, 1200, and 1800

mum channel cross section is $U_m=(\int_\Omega u dA)/(14bH)$, where the integration is taken over the entire area of the computational domain, Ω. The minimum channel hydraulic diameter is $D_H=2H$, and ν is the fluid kinematic viscosity. Other researchers have used the Orr-Sommerfeld definition of the Reynolds number, which is $Re_{OS}=(3/8)Re$ [2].

For Re=600, temperature contours lines in the open passage are virtually parallel to the x-axis. Streamline plots (not shown) indicate that the central portion of the passage has essentially no transverse motion and the grooves contain slowly turning vortices. The effect of the vortices on the contour lines in the grooves is evident. In contrast, long contiguously grooved channels exhibit two-dimensional waves for Re$\geqslant$350 [9,13,14]. The steady behavior of the current intermittently grooved passage indicates that the development length for unsteady flow at Re=600 is longer than the groove section length, $7b$. This result is consistent with the convective nature of the instability [10].

At Re=1200 a wavy structure develops in the third groove and its amplitude grows in the x-direction. This transverse motion persists for the remainder of the grooved section and for several groove-lengths into the flat region. At Re=1800, the transverse motion is stronger and more irregular than it is at Re=1200. It develops more rapidly in the grooved section and decays more slowly in the flat region.

Figure 3 shows contours plots of the root-mean-squared component of the dimensionless periodic temperature θ_{rms}, for Re =600, 1200, and 1800. While the isotherms for Re=600 in Fig. 2 are nearly parallel to the x-axis, Fig. 3 shows that some unsteadiness develops in the fifth groove and persists roughly three groove lengths into the flat region. This unsteadiness is concentrated in the region across the groove opening, and does not penetrate deeply into the grooves. The contour plots for Re=1200 and 1800 show that as the Reynolds number is increased, unsteadiness appears closer to the first groove and it persists further into the flat region. Moreover, the flow exhibits high levels of unsteadiness deep in the grooves. For Re=1800 a significant level of unsteadiness is present at the end of the flat section (entrance to the groove region).

Figure 4 shows dimensionless axial velocity unsteadiness u'/U_m versus location and Reynolds numbers. This unsteadiness is defined as $u'/U_m=(1/D_h)\int(u_{rms}/U_m)dy$, where u_{rms} is the root-mean-squared deviation of the axial velocity from its local time mean value, and the integration is taken from the bottom to the top of the channel. The region $0\leqslant x/b\leqslant 7$ corresponds to the grooved portion of the domain, while $7\leqslant x/b\leqslant 14$ represents the flat section. Two traces are included for Re=1800 with spectral orders of $N=7$ and 9.

At Re=600, the velocity unsteadiness reaches maximum values of less than 2 percent near the end of the grooved section. For Re=1200, the unsteadiness grows in the first four grooves ($0\leqslant x/b\leqslant 4$), drops off slightly in the next groove ($4\leqslant x/b\leqslant 5$), and then increases in the two last grooves. The unsteadiness remains near the high values observed in the grooved section for the first half-groove-length of the flat region. It drops off very rapidly for the next two groove-lengths and then decreases at a much slower rate. For Re=1800, the unsteadiness grows rapidly in the first three grooves, drops off in the fourth groove, grows again in the next two grooves and then drops off slightly in the last groove. Once again the unsteadiness remains high in the first half-groove-length of the flat region before dropping off. Time dependent streamline plots show that the velocity field exhibits a traveling wave structure. In Fig. 4, the local rises and dips in the time-averaged data indicate that the flow field exhibits standing waves as well.

The thinner solid lines in Fig. 5 show bulk Nusselt number versus axial location and Reynolds number. A dashed horizontal line in the region $7\leqslant x/b\leqslant 14$ shows the Nusselt number in a fully developed flat passage. The thicker line in the domain $5\leqslant x/b$

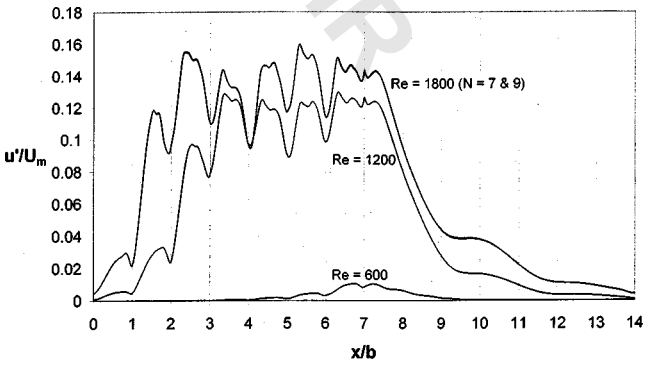

Fig. 4 Unsteady component of axial velocity versus location and Reynolds number

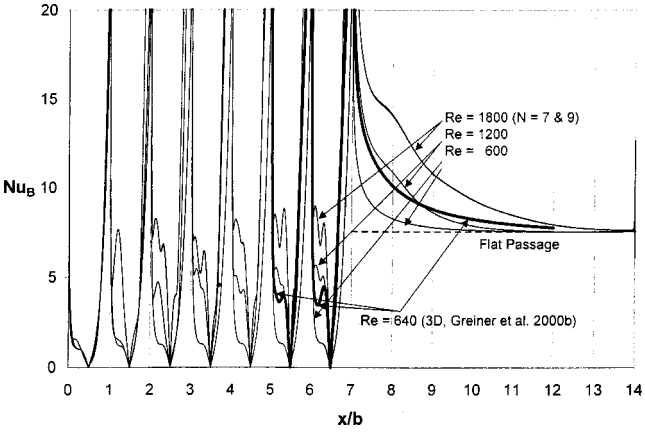

Fig. 5 Bulk Nusselt number versus location and Reynolds number

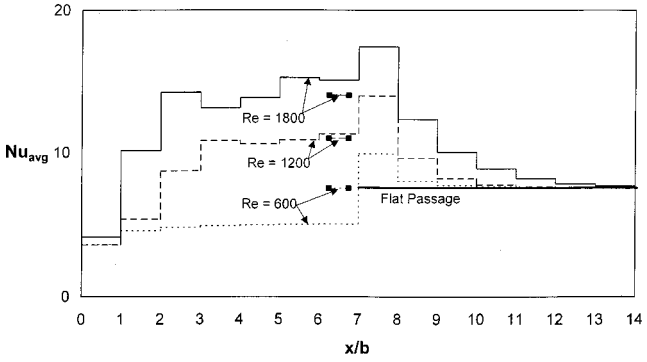

Fig. 6 Groove-length averaged Nusselt number versus location and Reynolds number

$\leqslant 12$ shows results at Re=640 from a *three-dimensional* simulation of a flat passage downstream of a *fully developed* grooved channel [17].

The bulk Nusselt number is defined as $\mathrm{Nu}_B=(D_h/k)\times(\langle q''/\Delta T_B\rangle)$, where the pointed brackets ($\langle\ \rangle$) indicate a time average. In this expression the fluid thermal conductivity is k and ΔT_B is the local temperature difference between the surface and bulk fluid. The bulk temperature at any axial location x and time t is defined as $T_B(x,t)=(\int uT\,dy)/(\int u\,dy)$, where both integrations in the y direction are taken from the bottom to the top of the domain. The heat transfer to the fluid per unit *projected* surface area is $q''(x,t)=-k(dT/dn)_{\mathrm{wall}}/m$, where T is temperature, n is the direction normal to the wall, m is the wall surface direction cosine, and the temperature gradient is evaluated at the wall. The direction cosine in the flat region is $m=1$, while it is $m=0.7071$ in the grooved region. Two traces are included for Re=1800 with spectral orders of $N=7$ and 9.

The strong singularities at $x/b=0$, 1, 2, 3, 4, 5, 6, and 7 are caused by the sharp edges of the groove peaks. At all other locations Nu_B increases with Reynolds number. The heat transfer in the first groove is very similar for all three Reynolds numbers. We see that the Nusselt number on the downstream (windward) surface ($0.5\leqslant x/b\leqslant 1$) is significantly higher than that on the upstream (leeward) side ($0\leqslant x/b\leqslant 0.5$). This is due to the location and rotation direction of the groove vortex flow. The upstream surface exhibits a local plateau centered at $x/b=0.3$. The groove vortex impinges against the wall at that location.

For Re=600, the shape of the Nusselt number profile is similar in all seven grooves. At Re=1200 the profile shape in the second groove is similar to that in the first. Its shape then changes substantially in subsequent grooves and its magnitude increases. The heat transfer on the windward side of each groove is greater than the level exhibited at Re=600. Moreover, the groove vortex impingement plateau grows stronger in the third through fifth groove. Its shape is essentially the same in the fifth, sixth and seventh grooves, indicating that the heat transfer has approached its fully developed condition. The profile shape has a number of local peaks especially on the leeward face. This suggests the time-averaged flow field has small secondary vortices that impinge against the walls at the locations of the peaks. For Re=1800, the Nusselt number profile in the second groove is substantially different form its shape in the first groove. Moreover, its shape does not appear to stabilize until the sixth or seventh groove, although it is difficult to say whether it would continue to change if the grooved section were longer.

The heat transfer at the inlet of the flat region ($x/b=7$) is well above the fully developed flat passage value for all three Reynolds numbers. Very steep velocity and temperature gradients near the walls cause this. The heat transfer for Re=600 drops to the flat passage value after three groove lengths as its wall gradients approach the fully developed levels. Examining the Re=1200 and 1800 traces shows that both the level of heat transfer enhancement and the length of the flat region where augmentation is observed increase with Reynolds number. The steeper velocity and temperature gradients as well as the higher levels of unsteadiness cause these increases. For Re=1200 and 1800, the heat transfer drop off is inflected one-half of a groove-length downstream from the grooved section. This corresponds to the location where the velocity unsteadiness in Fig. 4 begins to decrease. At Re=1800, heat transfer enhancement persists for the full length of the flat region.

The three-dimensional results for Re=640 (thicker line, Greiner et al. [17]) give heat transfer levels that are substantially higher than the current Re=600 data. As mentioned earlier, the three-dimensional results are for a flat passage downstream of a *fully developed* grooved channel. The flow in a fully developed grooved channel is unsteady for $\mathrm{Re}\geqslant 350$, while the current intermittently grooved passage is essentially steady at Re=600. The unsteady structure of the three-dimensional simulation increases the heat transfer level well beyond that predicted by the current work for Re=600. In fact, its level is closer to the current Re=1200 results. Moreover, the three-dimensional simulations do not predict the inflection at $x/b=7.5$ or the secondary vortices in the grooves.

Figure 6 shows the bulk Nusselt number averaged over different groove-length regions of the domain. A thicker solid line shows the fully developed flat passage Nusselt number. The horizontal line segments with solid squares represent *fully developed* grooved channel results from two-dimensional simulations at Re=600, 1200 and 1800 [14]. Those simulations employed a computational domain that represents one periodicity cell of the grooved channel and periodic inlet/outlet boundary conditions.

For Re=600 the average Nusselt number increases slightly for the first four grooves and then reaches a fully developed value. This value is below the flat passage level. The thermal resistance of the slowly turning groove-vortices causes this reduction in heat transfer. For Re=1200, the average heat transfer in the first groove is the same as that at Re=600, but its value increases substantially in the second, third and fourth grooves. After reaching a local maximum the heat transfer drops slightly in the fifth notch and then rises slightly in the sixth and seventh grooves. However, the heat transfer level in the last four groove-lengths is fairly uniform. Moreover, this level is greater than the value for a fully developed flat passage. The unsteady mixing at Re=1200 is sufficient to overcome the thermal resistance of the groove vortices.

At Re=1800 the heat transfer in the first groove is slightly higher than the level exhibited at Re=600 and 1200. This may be caused by the unsteadiness at the exit of the flat section (Figs. 3

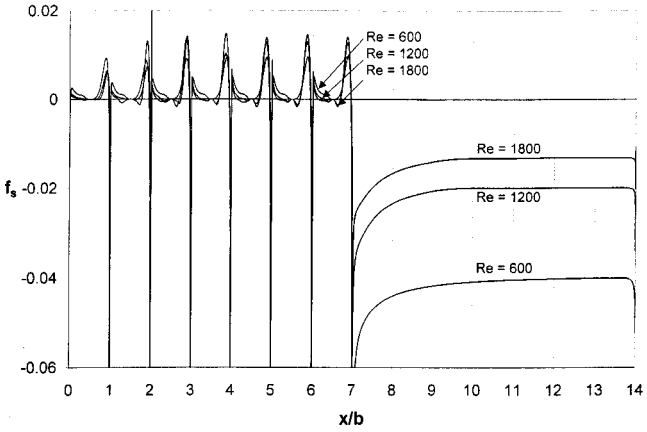

Fig. 7 Dimensionless axial shear stress versus location and Reynolds number

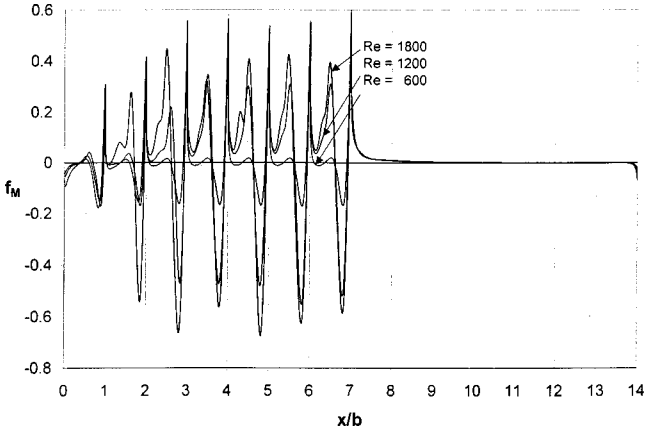

Fig. 8 Dimensionless momentum flux gradient versus location and Reynolds number

and 4). The heat transfer exhibits a substantial rise in the next two grooves. It drops in the fourth groove and rises for the next two grooves before dropping slightly in the final groove. The average Nusselt numbers in all but the first groove are greater than the fully developed flat passage value. The rise and fall of heat transfer in the interior grooves at Re=1200 and 1800 are closely correlated with the unsteady velocity levels described in Fig. 3.

At Re=600, the heat transfer in the seventh groove is substantially less than the level predicted for fully developed flow. The unsteadiness present in the fully developed simulation causes this difference. At Re=1200 and 1800 the heat transfer in the seventh groove is, respectively, 2 percent and 7 percent higher than the fully developed values.

In the flat region ($7 \leqslant x/b \leqslant 14$), the heat transfer begins at very high levels. It decreases as distance from the grooves increases, eventually approaching the fully developed rate. The heat transfer development length in the grooved region (as demonstrated by a rise in heat transfer) *decreases* as Reynolds number increases, while the heat transfer decay-length in the flat region *increases*. As a result, the length of the region of enhanced heat transfer increases with Reynolds number.

Figure 7 shows the dimensionless x-component of shear stress $f_S = 2\tau_x/\rho U_m{}^2$ versus axial location and Reynolds number. In this expression the x-component of wall shear stress is $\tau_x = -\mu(du_t/dn)_{\text{wall}}/m$, where u_t is time average component of fluid velocity tangential to the wall, ρ is the fluid density, and μ is the fluid dynamic viscosity. The strong negative singularities are caused by the sharp groove peaks at $x/b = 0$, 1, 2, 3, 4, 5, 6, and 7.

For Re=600, the shape of the shear stress profile in the grooves ($0 \leqslant x/b \leqslant 7$) has a number of similarities to the Nusselt number profiles seen in Fig. 5. For instance, the shear stress is significantly higher on the downstream surface of each groove than it is on the upstream side. Moreover, the shear stress exhibits a plateau 0.3-groove-lengths downstream from the leading edge of each groove. These similarities are caused by the analogous behavior of heat and momentum transport in the absence of strong pressure gradients.

At Re=600 the shear stress is positive throughout the grooved region (with the exception of the singular points). This indicates that the fluid near the groove surfaces is always moving in the negative x-direction. For Re=1200 and 1800, on the other hand, the shear stress is negative in certain locations. This implies that fluid in these regions moves in the *positive* x-direction, indicating the existence of secondary vortices, as described in connection with Fig. 5. In the flat region downstream of the grooves, the dimensionless shear stress is in the negative x-direction. The magnitude of the shear stress in the flat region is much higher than it is in the grooved region.

Comparing Figs. 5 and 7 shows that the wall shear stress is analogous to heat transfer. However, the *pressure gradient* is the drag characteristic that affects the pumping power per unit passage volume required of the prime mover, $(dp/dx)U_m$. This prime mover power is of great importance to many engineering devices. We now relate the Fanning pressure gradient $f_P = (-dF_p/dx)(1/2\rho U_m{}^2)$ to the wall shear stress. In this expression the time averaged pressure force is $F_p = \langle \int p\, dy \rangle$, where p is the local pressure and the integration is performed from the top to the bottom of the channel. A time-averaged force balance on a control volume of axial length dx shows that the Fanning pressure gradient is composed of wall shear stress and momentum flux gradient components, that is $f_P = f_M - f_S$. The axial gradient of the momentum flux is defined as $f_M = d/dx[\int(\langle u^2 \rangle/U_m{}^2)dy]$, where $\langle u^2 \rangle$ is the time average of the square of the x-velocity, and the integration is performed from the bottom to the top of the passage.

Figure 8 shows the axial gradient of the momentum flux f_M versus location and Reynolds number. In the first groove, the momentum flux gradient is similar for all three Reynolds numbers. In subsequent grooves, the magnitude of f_M increases with Reynolds numbers. This indicates that the fluid experiences large levels of acceleration and deceleration. In the flat region downstream of the grooves, the axial variation of the velocity is small and f_M drops to zero very quickly. Comparing Figs. 7 and 8 (and noting the y-axis scales), we see that the magnitude of the momentum flux gradient is much larger than that of the shear stress in the grooved regions, while the opposite is true in the flat portion of the passage. The local Fanning pressure gradient is the difference between the traces in these figures, $f_P = f_M - f_S$.

Figure 9 shows the product $f_{P,\text{avg}}\text{Re}$ versus location and Rey-

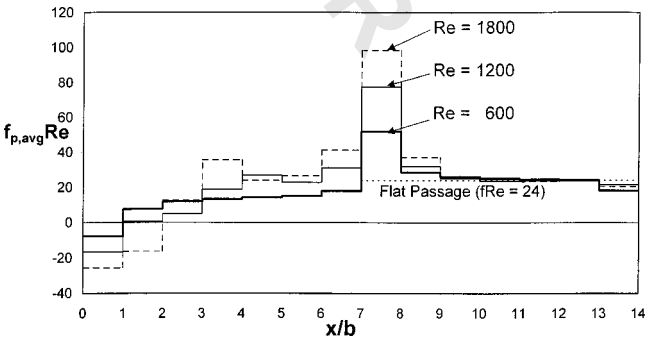

Fig. 9 Groove-length average Fanning pressure gradient versus location and Reynolds number

nolds number. In this product, $f_{P,\mathrm{avg}}$ is the Fanning pressure gradient averaged over different groove-length regions. The dotted horizontal line in the region $7 \leqslant x/b \leqslant 14$ shows the fully developed flat channel value $f_{P,\mathrm{avg}}\,\mathrm{Re}=24$. In the first groove $f_{P,\mathrm{avg}}\,\mathrm{Re}$ is negative for all three Reynolds numbers indicating that the dimensional pressure actually *increases* across this region. This pressure rise is caused by fluid deceleration. The expansion of the channel cross section as the flow exits a flat passage and enters the grooved region causes this deceleration. For $\mathrm{Re}=600$, the friction factor becomes positive in the second groove and continues to increase with distance from the inlet of the grooved section. The increment in $f_{P,\mathrm{avg}}\,\mathrm{Re}$ decreases with increasing x/b until the last groove. The pressure decrease across the last groove is larger than in the internal grooves because the flow accelerates as it exits the grooved section and enters the flat region.

For $\mathrm{Re}=1200$, $f_{P,\mathrm{avg}}\,\mathrm{Re}$ increases for the first five grooves, then decreases in the next groove, and finally increases in the last groove. The pressure gradient for $\mathrm{Re}=1800$ increases for the first four grooves, decreases in the next groove, and rises in the final two grooves. We see that the pressure gradient development length in the grooved section decreases with Reynolds number.

In the first groove-length of the flat region, $f_{P,\mathrm{avg}}\,\mathrm{Re}$ is very high for all three Reynolds numbers due to the high shear stress (sharp velocity gradients) at $x/b=7$. The pressure gradients then approach their fully developed values after only three groove lengths. The pressure gradient in the last groove-length of the flat region is below the fully developed flat passage value. This is due to the decelerating flow caused by the expanding cross sectional area at $x/b=14$.

Comparing Figs. 6 and 9, we see that while the heat transfer remains enhanced for up to six groove-lengths in the flat region, the pressure gradient drops back to the flat passage value in only three groove lengths. Moreover, while the decay length for heat transfer increases with Reynolds numbers, the pressure gradient decay length is rather insensitive to Reynolds number.

Conclusions

Two-dimensional Navier-Stokes simulations of heat and momentum transport in an intermittently grooved passage were performed using the spectral element technique for the Reynolds number range $600 \leqslant \mathrm{Re} \leqslant 1800$. The computational domain had seven contiguous transverse grooves cut symmetrically into opposite walls, followed by a flat section of the same length. This domain employed periodic inflow/outflow boundary conditions.

The flow is essentially steady at $\mathrm{Re}=600$. However, traveling waves develop near the inlet of the grooved section at $\mathrm{Re}=1200$ and 1800 and persist several groove lengths into the flat region. The axial variation of unsteady velocity within the grooved section is closely correlated with increases in heat transfer, shear stress and pressure gradient. In the grooved region the development lengths for heat transfer and pressure gradient both decrease with increasing Reynolds number. While the length of the flat region where heat transfer augmentation is observed increases with Reynolds number, the pressure gradient returns to the flat passage value in roughly three groove lengths for the entire Reynolds number range considered in this work.

The current two-dimensional simulations in an intermittently grooved passage exhibit a number of differences from three-dimensional results in fully developed grooved channels and downstream flat passages. However the current calculations will provide guidance for future three-dimensional calculations in intermittently grooved passages. Finally, these results suggest that intermittently grooved passages may offer very favorable heat transfer versus pumping power performance for engineering devices.

Acknowledgments

National Science Foundation Grant CTS-9501502 supported this work. The work of P.F. Fischer was supported by the Mathematical, Information, and Computational Sciences Division subprogram of the Office of Advanced Scientific Computing Research, U.S. Department of Energy, under Contract W-31-109-Eng-38. The work of H.M. Tufo was supported by the Department of Energy under Grant number B341495 to the Center on Astrophysical Thermonuclear Flashes at University of Chicago, and by the University of Chicago.

Nomenclature

b = groove length
c = decay constant
d = groove depth
D_h = minimum hydraulic diameter, $2H$
f_M = dimensionless momentum flux gradient
f_P = fanning pressure gradient
f_S = dimensionless axial shear stress
f_x = fluid body force per unit mass in the x-direction
H = minimum channel wall to wall spacing
k = fluid thermal conductivity, 0.0263 W/m°C
K = number of spectral elements
L_d = domain length, $14b$
N = spectral element order
Nu_B = bulk Nusselt number based on projected area
Pr = fluid molecular Prandtl number, 0.70
Re = reynolds number, $U_m D_h/\nu$
t = time
T = temperature
T_b = bulk temperature
u, v = velocity components in the x and y directions
u' = axial velocity unsteadiness
U_m = mean x-velocity at the minimum channel cross-section

Greek

α = thermal diffusivity, 2.63×10^{-5} m^2/s
ν = fluid kinematic viscosity, 1.84×10^{-5} m^2/s
θ = periodic temperature
ρ = fluid density, 1.006 kg/m^3
τ = period of local time variations
τ_x = x-component of wall shear stress
Ω = computation domain

References

[1] Webb, R. L., 1994, *Principles of Enhanced Heat Transfer*, John Wiley & Sons, New York.
[2] Ghaddar, N. K., Korczak, K., Mikic, B. B., and Patera, A. T., 1986, "Numerical Investigation of Incompressible Flow in Grooved Channels. Part 1: Stability and Self-Sustained Oscillations," J. Fluid Mech., **168**, pp. 541–567.
[3] Greiner, M., 1991, "An Experimental Investigation of Resonant Heat Transfer Enhancement in Grooved Channels," Int. J. Heat Mass Transf., **24**, pp. 1383–1391.
[4] Roberts, E. P. L., 1994, "A Numerical and Experimental Study of Transition Processes in an Obstructed Channel Flow," J. Fluid Mech., **260**, pp. 185–209.
[5] Lee, B. S., Kang, I. S., and Lim, H. C., 1999, "Chaotic Mixing and Mass Transfer Enhancement by Pulsatile Laminar Flow in an Axisymmetric Wavy Channel," Int. J. Heat Mass Transf., **42**, pp. 2571–2581.
[6] Kozlu, H., Mikic, B. B., and Patera, A. T., 1988, "Minimum-Dissipation Heat Removal by Scale-Matched Flow Destabilization," Int. J. Heat Mass Transf., **31**, pp. 2023–2032.
[7] Karniadakis, G. E., Mikic, B. B., and Patera, A. T., 1988, "Minimum-Dissipation Transport Enhancement by Flow Destabilization: Reynolds Analogy Revisited," J. Fluid Mech., **192**, pp. 365–391.
[8] Amon, C. H., Majumdar, D., Herman, C. V., Mayinger, F., Mikic, B. B., and Sekulic, D. P., 1992, "Experimental and Numerical Investigation of Oscillatory Flow and Thermal Phenomena in Communicating Channels," Int. J. Heat Mass Transf., **35**, pp. 3115–3129.
[9] Greiner, M., Chen, R.-F., and Wirtz, R. A., 1990, "Heat Transfer Augmentation Through Wall-Shaped-Induced Flow Destabilization," J. Heat Transfer , **112**, pp. 336–341.
[10] Schatz, M. F., Tagg, R. P., Swinney, H. L., Fischer, P. F., and Patera, A. T., 1991, "Supercritical Transition in Plane Channel Flow with Spatially Periodic Perturbations," Phys. Rev. Lett., **66**, No. 12, pp. 1579–1582.
[11] Greiner, M., Chen, R.-F., and Wirtz, R. A., 1991, "Enhanced Heat Transfer/Pressure Drop Measured From a Flat Surface in a Grooved Channel," J. Heat Transfer, **113**, pp. 498–500.

[12] Wirtz, R. A., Huang, F., and Greiner, M., 1999, ''Correlation of Fully Developed Heat Transfer and Pressure Drop in a Symmetrically Grooved Channel,'' J. Heat Transfer, **121**, pp. 236–239.
[13] Greiner, M., Spencer, G., and Fischer, P. F., 1998, ''Direct Numerical Simulation of Three-Dimensional Flow and Augmented Heat Transfer in a Grooved Channel,'' J. Heat Transfer, **120**, pp. 717–723.
[14] Greiner, M., Faulkner, R. J., Van, V. T., Tufo, H. M., and Fischer, P. F., 2000, ''Simulations of Three-Dimensional Flow and Augmented Heat Transfer in a Symmetrically Grooved Channel with Constant Temperature Walls,'' J. Heat Transfer, **122**, pp. 653–660.
[15] Greiner, M., Chen, R.-F., and Wirtz, R. A., 1995, ''Augmented Heat Transfer in a Recovery Passage Downstream From a Grooved Section: An Example of Uncoupled Heat/Momentum Transport,'' J. Heat Transfer, **117**, pp. 303–308.
[16] Huang, F., 1998, ''Experimental Investigation of Fully-Developed Augmented Convection in a Symmetrically Grooved Channel,'' Masters of Science Degree thesis, University of Nevada, Reno, NV, May 1998.
[17] Greiner, M., Fischer, P. F., Tufo, H. M., and Wirtz, R. A., 2001, ''Three Dimensional Simulations of Enhanced Heat Transfer in a Flat Passage Downstream From a Grooved Channel,'' J. Heat Transfer, **124**(1), pp. 169–176.
[18] Patera, A. T., 1984, ''A Spectral Element Method for Fluid Dynamics; Laminar Flow in a Channel Expansion,'' J. Comp. Phys., **54**, pp. 468–488.
[19] Maday, Y., and Patera, A. T., 1989, ''Spectral Element Methods for the Navier-Stokes Equations,'' *State of the Art Surveys on Computational Mechanics*, A. K. Noor and J. T. Oden, eds., ASME, New York, pp. 71–143.
[20] Fischer, P. F., 1997, ''An Overlapping Schwarz Method for Spectral Element Solution of the Incompressible Navier-Stokes Equations,'' J. Comp. Phys., **133**, pp. 84–101.
[21] Ghaddar, N. K., Karniadakis, G. E., and Patera, A. T., 1986, ''A Conservative Isparametric Spectral Element Method for Forced Convection: Application to Fully Developed Flow in Periodic Geometries,'' Numer. Heat Transfer, **9**, pp. 277–300.
[22] Fischer, P. F., and Patera, A. T., 1992, ''Parallel Spectral Element Solutions of Eddy-Promoter Channel Flow,'' *Proc. of the European Research Community on Flow Turbulence and Computation Workshop*, Lausanne, Switzerland, Cambridge University Press, pp. 246–256.
[23] Patankar, S. V., Liu, C. H., and Sparrow, E. M., 1977, ''Fully Developed Flow and Heat Transfer in Ducts Having Streamwise Periodic Variations of Cross-Sectional Area,'' J. Heat Transfer, **99**, pp. 180–186.
[24] Kays, W. M., and Crawford, M. E., 1993, *Convection Heat and Mass Transfer*, 3rd edition, McGraw-Hill, New York.
[25] Fischer, P. F., and Patera, A. T., 1991, ''Parallel Spectral Element Solutions of the Stokes Problem,'' J. Comp. Phys. **92**, pp. 380–421.

PROOF COPY 007203JHR